

# Effect of Annealing Temperature on Microstructure and Shape Memory Characteristics of Ti–22Nb–6Zr(at%) Biomedical Alloy

Jae Il Kim<sup>1,2</sup>, Hee Young Kim<sup>1</sup>, Tomonari Inamura<sup>3</sup>, Hideki Hosoda<sup>3</sup> and Shuichi Miyazaki<sup>1,\*</sup>

<sup>1</sup>*Institute of Materials Science, University of Tsukuba, Tsukuba 305-8573, Japan*

<sup>2</sup>*Materials Science and Engineering, Dong-A University, Busan 604-714, Korea*

<sup>3</sup>*Precision and Intelligence Laboratory, Tokyo Institute of Technology, Yokohama 226-8503, Japan*

Effect of annealing temperature on microstructure and shape memory characteristics of Ti–22Nb–6Zr(at%) biomedical alloys was investigated by using tensile tests, XRD measurement, scanning electron microscopy (SEM) and transmission electron microscopy (TEM). After severe cold-rolling, the plate was annealed at temperatures between 773 and 1173 K. The  $\alpha/\beta$  transus temperature in this alloy was determined to be between 823 and 873 K. The specimen annealed at 823 K for 3.6 ks exhibited a fine subgrain structure. A fully recrystallized structure was observed in the specimens annealed above 873 K. The annealing temperature less affected the transformation temperature and recovery strain. However, the critical stress for slip decreased considerably with increasing annealing temperature, because the grain size increased. All specimens annealed above 823 K exhibited stable superelastic behavior at room temperature.

(Received November 4, 2005; Accepted December 21, 2005; Published March 15, 2006)

**Keywords:** *shape memory effect, superelasticity, biomaterials, titanium based alloy, titanium–niobium–zirconium, Hall–Petch relationship*

## 1. Introduction

Ti-based alloys have been applied as biomedical materials to date due to their high corrosion resistance, high biocompatibility and low Young's modulus. Among biomedical alloys, Ti–Ni alloys have been applied as orthodontic arch wires, bone plates and stents, owing to their unique shape memory effect and superelasticity. However, it has been reported that pure Ni is a toxic element and causes Ni-hypersensitivity.<sup>1)</sup> Although clear Ni-hypersensitivity to human body in Ti–Ni alloys has not been reported until now, it is preferable to develop absolutely safe Ni-free Ti-based shape memory alloys for biomedical applications.

Many  $\beta$ -type Ti-based alloys have been investigated to date, e.g., Ti–V based alloys,<sup>2)</sup> Ti–Mo based alloys<sup>3–8)</sup> and Ti–Nb based alloys<sup>9–15)</sup> since Baker reported the shape memory effect in a Ti–35 mass%Nb alloy.<sup>9)</sup> Considering biomedical applications, the Ti–V based alloys are not suitable because of cytotoxicity of V.<sup>16)</sup> The shape memory effect in the Ti-based alloys may be affected by the following factors; (1) aging treatment, which may cause precipitation hardening due to  $\alpha$  phase and  $\omega$  phase and (2) thermo-mechanical treatment (cold work followed by annealing), which may improve shape memory characteristics by dense dislocations and grain refinement. The fine thermal  $\omega$  precipitates formed by aging treatment improve the shape memory properties, because they increase the critical stress for slip. On the other hand, it is known that grain refinement *via* cold working followed by low temperature annealing may be useful method for improving mechanical properties of alloys. However, no systematic research on the effect of annealing condition on the shape memory characteristics has been carried out in the  $\beta$ -type Ti-based alloys to date.

Recently, the effect of Zr addition to the Ti–Nb alloy on shape memory characteristics has been reported.<sup>15)</sup> According to this study, a solution-treated Ti–22Nb–6Zr(at%) alloy exhibits superior superelastic behavior at room temperature

than Ti–Nb binary alloys. In the present study, in order to improve shape memory characteristics of Ti–22Nb–6Zr(at%) alloy, the effect of annealing temperature on shape memory characteristics were investigated by tensile tests at various temperatures, XRD (X-ray diffraction) measurement, scanning electron microscopy (SEM) and transmission electron microscopy (TEM).

## 2. Experimental

A Ti–22Nb–6Zr(at%) ingot was fabricated by an Ar arc melting method. The ingot was cold-rolled to a plate of 0.5 mm in thickness with a final cold working ratio of 95%. Specimens for XRD measurement, tensile tests, SEM observation and TEM observation were cut from the plate by an electro-discharge machine. All the specimens were finally annealed at 773, 823, 873, 973, 1073 K for 3.6 ks and 1173 K for 1.8 ks in an Ar atmosphere, followed by quenching into water. After the annealing treatment, the specimens were etched in order to remove oxidized surface. In order to investigate the shape memory characteristics, tensile tests were carried out at a strain rate of  $1.67 \times 10^{-4} \text{ s}^{-1}$  at various temperatures. The gage length of specimens for tensile tests was 20 mm. XRD measurement was conducted at room temperature with Cu K $\alpha$  radiation to determine the constituent phases. Specimen for TEM observation were prepared by a conventional twin-jet polishing technique using an electrolyte solution of 5 vol% sulfuric acid, 2 vol% hydrofluoric acid and 93 vol% methanol at 230 K. The TEM observation was conducted using a JEOL2010F microscope operated at 200 kV. Grain size was measured using SEM micrographs.

## 3. Results and Discussion

### 3.1 Effect of annealing temperature on microstructure

In order to identify the constituent phases of each annealed specimens at room temperature, X-ray diffraction measurement was carried out. Figure 1 shows X-ray diffraction

\*Corresponding author, E-mail: miyazaki@ims.tsukuba.ac.jp

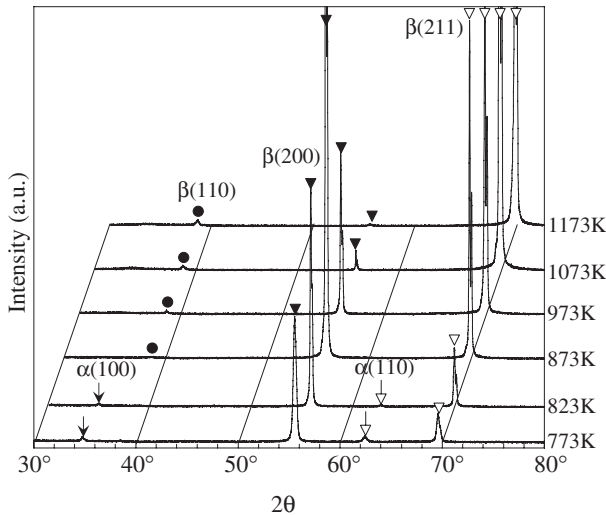


Fig. 1 XRD profiles measured at room temperature in the specimens annealed at temperatures between 773 and 1173 K.

profiles of the specimens annealed at temperatures between 773 and 1173 K. Within the  $2\theta$  range shown in this figure, the  $\alpha$  phase is identified by two major reflections from  $(100)_\alpha$  and  $(110)_\alpha$ , whereas the  $\beta$  phase is identified by three major reflections. Comparing with the intensities of  $\{211\}_\beta$  peak in the specimens annealed at 773 and 823 K, those of  $\{200\}_\beta$  peak are very strong. It is assumed that this is due to a deformation texture. Kim *et al.*<sup>17)</sup> reported that a well developed  $\{100\}\langle 110\rangle$  texture was obtained in as-rolled and annealed Ti-22Nb-6Ta alloys after severe cold-rolling. On the other hand, the intensities of  $\{211\}_\beta$  peak are stronger

than those of  $\{200\}_\beta$  peak in the specimens annealed at 1073 and 1173 K. This is due to a recrystallization texture. It has been also reported that a recrystallization texture of  $112\langle 110\rangle$  is developed in Ti-22Nb-6Ta<sup>17)</sup> and Ti-22Nb-3Al<sup>18)</sup> alloys heat treated at 1173 and 1273 K, respectively, after severe cold-rolling. Based on previous researches<sup>17,18)</sup> and present XRD results, it is expected that the deformation and recrystallization texture of Ti-22Nb-6Zr alloy exhibit similar one as those of other Ti-Nb based alloys. It is also noted that both of the  $\{200\}_\beta$  peak and  $\{211\}_\beta$  peak are strong in the specimen annealed at 873 K for 3.6 ks, indicating that the deformation and recrystallization textures coexist.

While the diffraction peaks corresponding to the  $\alpha$  phase are observed in the specimens annealed at 773 and 823 K, there exist only the peaks corresponding to the  $\beta$  phase in the specimens annealed above 873 K. This means that the  $\alpha/\beta$  transus temperature of this alloy is between 823 and 873 K. According to the Ti-Nb binary phase diagram, the  $\alpha/\beta$  transus temperature of Ti-22Nb is about 830 K. This indicates that the addition of Zr does not affect the  $\alpha/\beta$  transus temperature significantly. On the other hand, the peaks corresponding to  $\alpha''$  can not be observed in any specimen. This indicates that the martensitic transformation start temperature ( $M_s$ ) of these specimens is below room temperature.

Figure 2 shows the microstructures observed by SEM in the specimens annealed at 873, 973, 1073 and 1173 K. It is also clear that no martensite phase ( $\alpha''$ ) was observed in all annealed specimens. As shown in these figures, any secondary phase can not be observed. The results of these SEM micrographs are well consistent with those of the XRD

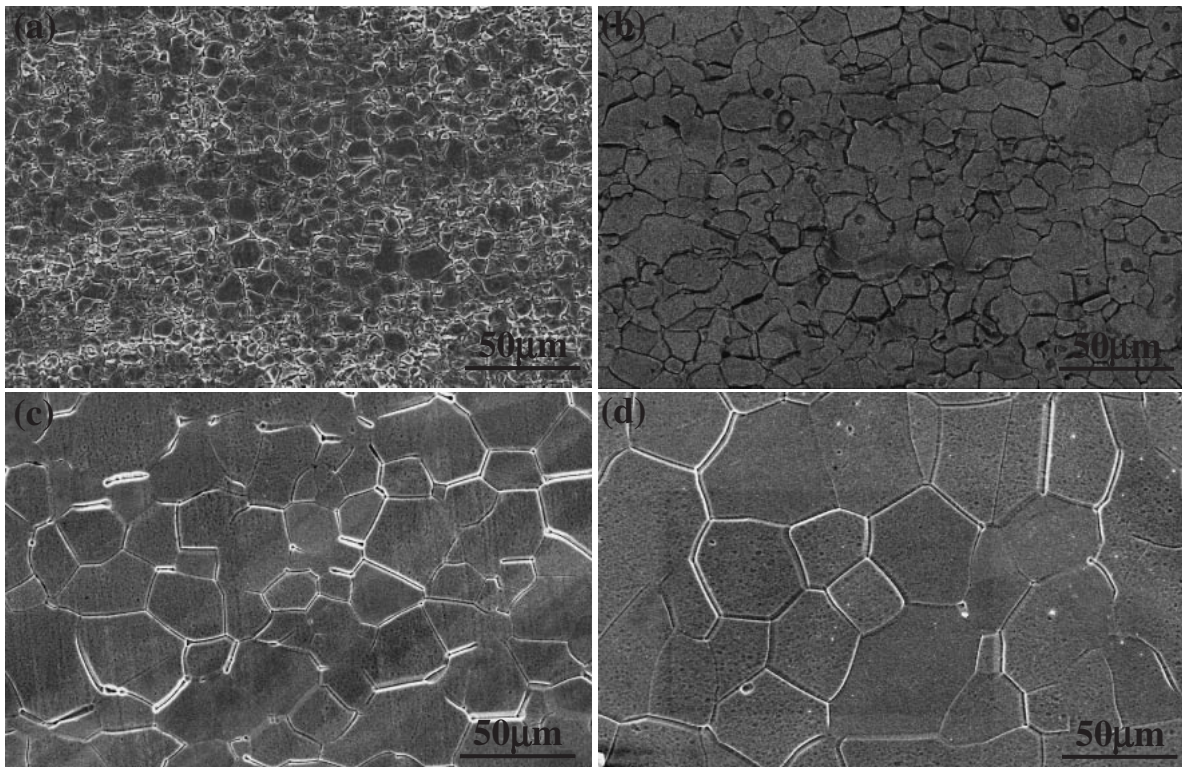


Fig. 2 SEM micrographs of the specimens annealed at (a) 873 K, (b) 973 K, (c) 1073 K and (d) 1173 K.



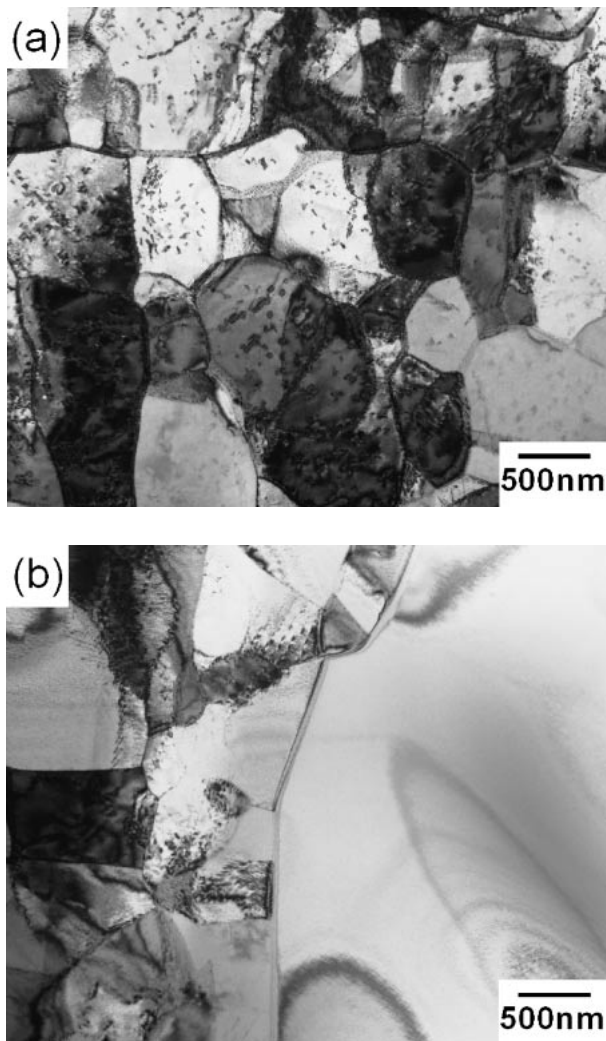


Fig. 3 TEM bright field micrographs of the specimens annealed at (a) 823 K and (b) 873 K.

measurement. Figure 3 shows the bright field TEM micrographs of the specimens annealed at (a) 823 K and (b) 873 K. In the specimen annealed at 823 K, the subgrains with size of about  $1.5\ \mu\text{m}$  are observed and the secondary phase is also observed. This secondary phase is identified to be  $\alpha$  phase as shown in Fig. 4. On the other hand, a bimodal grain structure consisting of fine subgrains and large recrystallized grains is observed in the specimen annealed at 873 K as shown in Fig. 3(b). No secondary phase is observed in the specimen annealed at 873 K.

Figure 4 shows bright field images and the corresponding selected area diffraction patterns (SADP) in the specimens annealed at (a) 823 K, (b) 873 K and (c) 973 K. Figure 4(d) shows the key diagram corresponding to Fig. 4(a). The beam directions are parallel to  $[100]$  of  $\beta$  phase. As shown in Fig. 4(a), the secondary phase with size of 30 nm can be seen in the grains. In the SADP, diffuse spots at  $1/2\{110\}_\beta$  and  $1/2\{013\}_\beta$  can be seen in addition to primary reflections from  $\beta$  phase. These spots can be identified to be  $\alpha$  phase in Fig. 4(a). On the other hand, the  $\alpha$  phase can not be detected in the specimens annealed at 873 and 973 K as shown in Figs. 4(b) and (c). These results of TEM observation are well consistent with the XRD measurement.

Figure 5 shows dark field TEM micrographs and the corresponding SADP of the specimens annealed at (a) 823 K, (b) 873 K and (c) 973 K. All SADPs were obtained from  $[110]_\beta$  zone axis. In all SADPs, diffuse scattering at  $1/3\{112\}_\beta$  positions corresponding to the  $\omega$  phase can be seen in addition to the primary reflections from  $\beta$  matrix. The spot indicated by a circle in each SADP was used to take the corresponding dark field micrograph. Dispersion of very fine  $\omega$  particles with a dimension of 3 nm was observed in all dark field micrographs. It is clear that the density and size of the  $\omega$  phase do not depend on annealing temperature. The  $\omega$  phase is athermal one formed during quenching, since the thermal  $\omega$  phase is formed by aging below 698 K in Ti–Nb alloys.<sup>19)</sup>

The grain size was measured using SEM micrographs and it is plotted against the annealing temperature in Fig. 6. The grain size was measured by a linear intercept method. Based on the TEM observation, the subgrain size of the specimen annealed at 823 K, about  $1.5\ \mu\text{m}$ , was also plotted. The grain size increases with increasing annealing temperature to  $40\ \mu\text{m}$  at 1173 K.

### 3.2 Effect of annealing temperature on shape memory properties

Figure 7 shows stress–strain curves of the specimens annealed at temperatures between 773 and 1173 K. The tensile tests were carried out at room temperature. The specimens annealed at temperatures between 823 and 1173 K exhibit a two-stage yielding. The first stage yielding indicated by a black-headed arrow corresponds to the deformation of the stress-induced martensitic transformation because the  $M_s$  of these specimens is below room temperature as shown in the XRD measurement, SEM and TEM observation. The second stage yielding indicated by a white-headed arrow corresponds to the starting point of plastic deformation. The specimens annealed at 773 K exhibits a single-stage yield. Therefore, this specimen starts plastic deformation prior to the stress induced martensitic transformation. The fracture stresses and fracture strains were evaluated using the stress–strain curves of all the specimens, and they are plotted against annealing temperature in Fig. 8. The fracture stress decreases from 720 to 420 MPa with increasing annealing temperature from 773 to 873 K, and then exhibits similar values in the specimens annealed at temperatures between 873 and 1173 K. On the other hand, the fracture strain increases with increasing annealing temperature from 7 to 29% due to the recovery and recrystallization.

In order to determine the martensitic transformation temperature, tensile tests were carried out at various temperatures. Figure 9 shows a series of stress–strain curves obtained at various temperatures for the specimens annealed at 873 K. All the specimens were deformed to a strain of 2.5% followed by unloading. All the specimens were heated up to 500 K (above the reverse martensitic transformation finish temperature;  $A_f$ ) after unloading; lines with an arrow indicate the shape recovery by heating. The yield point, indicated by a larger arrow, is determined at the intersection of the stress–strain curve and a line parallel to the initial elastic portion of the stress–strain curve but offset by 0.2% from the origin as shown in Fig. 9. The shape memory effect was mainly observed for the specimens deformed at temperatures

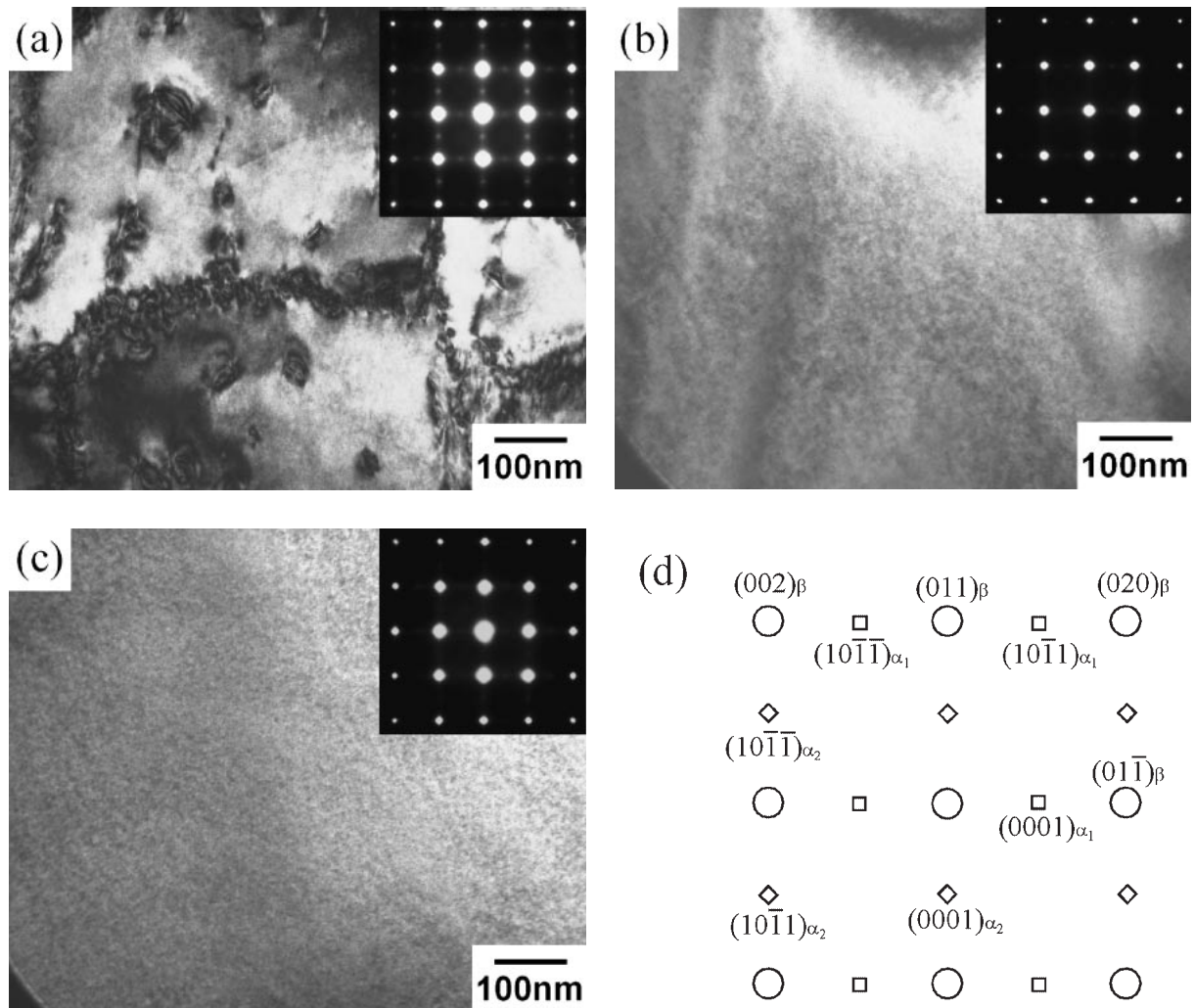


Fig. 4 TEM bright field micrographs and the corresponding diffraction patterns in the specimens annealed at (a) 823 K, (b) 873 K and (c) 973 K, (d) being a key diagram of the diffraction pattern.

between 173 and 233 K. The residual strain after unloading was recovered by heating. The superelastic behavior was mainly observed for the specimens deformed at temperatures between 253 and 313 K. However, the superelastic strain upon unloading decreases with increasing test temperature above 298 K. The yield stress for each curve was plotted as a function of test temperature in Fig. 10. The results of other specimens annealed at various temperatures were also plotted in this figure. The yield stress in all specimens decreases with increasing test temperature to the minimum, and increases with further increasing test temperature. In general, the temperature exhibiting the minimum yield stress is taken as the martensitic transformation start temperature ( $M_s$ ); e.g.,  $M_s$  of the specimen annealed at 873 K is determined to be 233 K. As shown in this figure, the  $M_s$  in all specimens were determined to be between 213 and 233 K irrespective of annealing temperature. According to these experimental results, it is confirmed that the  $M_s$  temperature is less affected by annealing temperature between 873 and 1173 K.

Figure 11 shows stress–strain curves of a specimen annealed at 873 K. Each stress–strain curve and recovery strain was obtained at room temperature by a loading and unloading cycle followed by heating: the strain recovery by

heating being indicated by a broken arrow. The similar measurement was repeated by increasing the maximum strain by 0.5% upon loading in the same specimen. In order to characterize the shape memory behavior of the specimen, four types of strains are defined as follows; (1) the permanently remained strain  $\varepsilon_P$  after unloading followed by subsequent heating, (2) the elastic strain  $\varepsilon_E$  recovered elastically upon unloading, (3) the recovered strain  $\varepsilon_{Tr}$  due to the reverse transformation, i.e., the summation of the strain recovered superelastically upon unloading and strain recovered by heating and (4) the total recovered strain  $\varepsilon_{Tot}$  consisting of  $\varepsilon_{Tr}$  and  $\varepsilon_E$ . Almost complete superelastic behavior was observed in the first six curves, while the strain recovery by heating above  $A_f$  temperature in addition to the superelastic strain recovery was observed after the 7th cycle. The plastic strain increases with increasing applied strain upon loading. Similar cyclic tensile tests were also carried out for other specimens.

The  $\varepsilon_E$ ,  $\varepsilon_{Tr}$  and  $\varepsilon_{Tot}$  estimated in Fig. 11 were plotted against the applied stress in Fig. 12. The  $\varepsilon_P$  starts to increase from 422 MPa. The  $\varepsilon_{Tr}$  and  $\varepsilon_{Tot}$  increase to the maximum with increasing stress and saturate with further increasing stress. Generally speaking, the shape memory behavior can

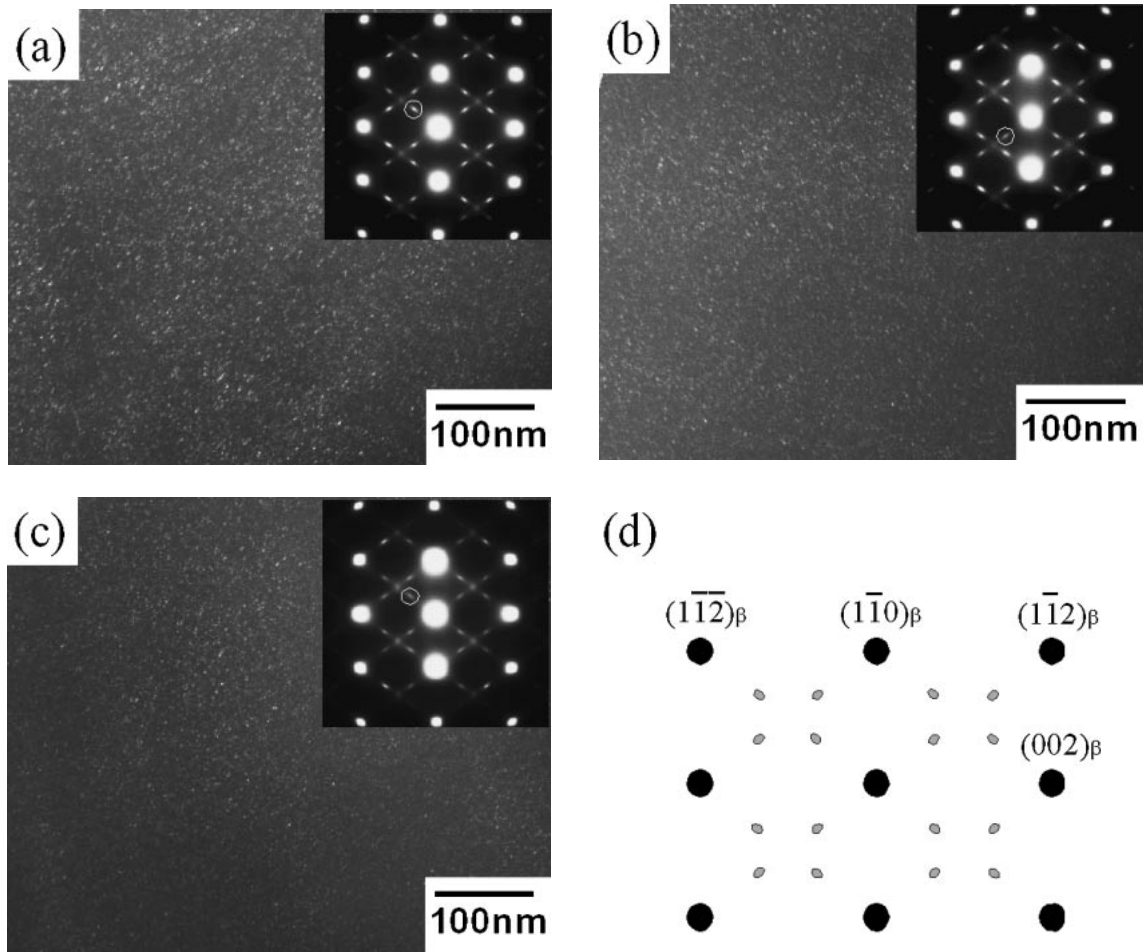


Fig. 5 TEM dark field images and the corresponding diffraction patterns in the specimens annealed at (a) 823 K, (b) 873 K and (c) 973 K, (d) being a key diagram of the diffraction pattern.

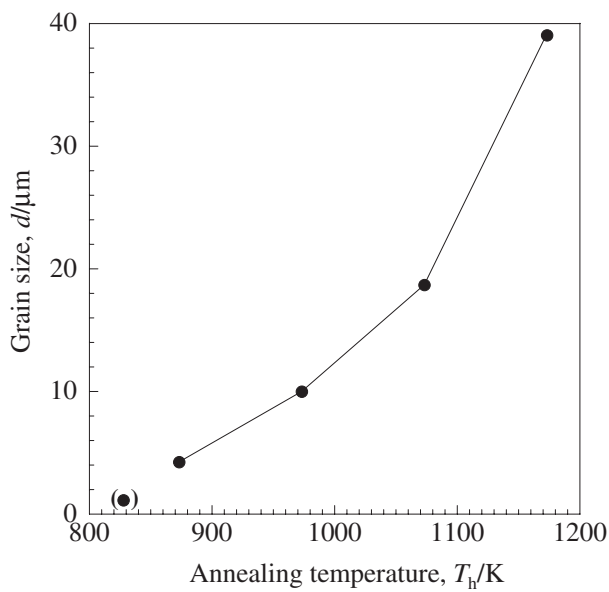


Fig. 6 Annealing temperature dependence of grain size in the specimens annealed at temperatures between 823 and 1173 K.

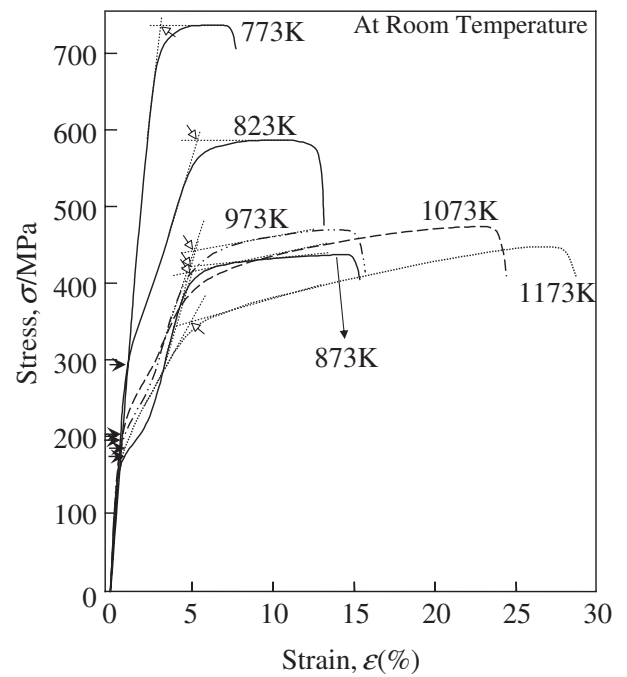


Fig. 7 Stress-strain curves obtained at room temperature in the specimens annealed at temperatures between 773 and 1173 K.



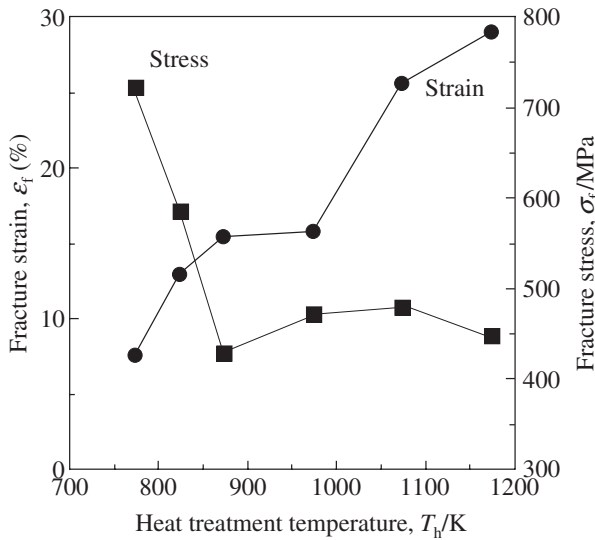


Fig. 8 Effect of annealing temperature on fracture stress and fracture strain in the specimens annealed at temperatures between 773 and 1173 K.

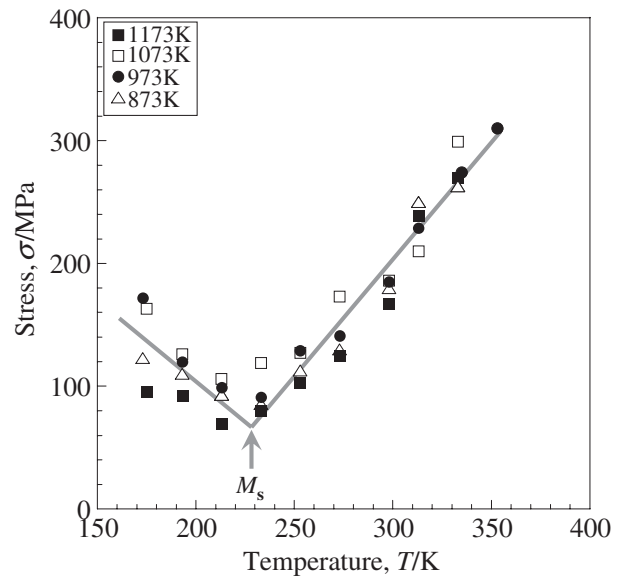


Fig. 10 Test temperature dependence of critical yield stress in the specimens annealed at temperatures between 773 and 1173 K.

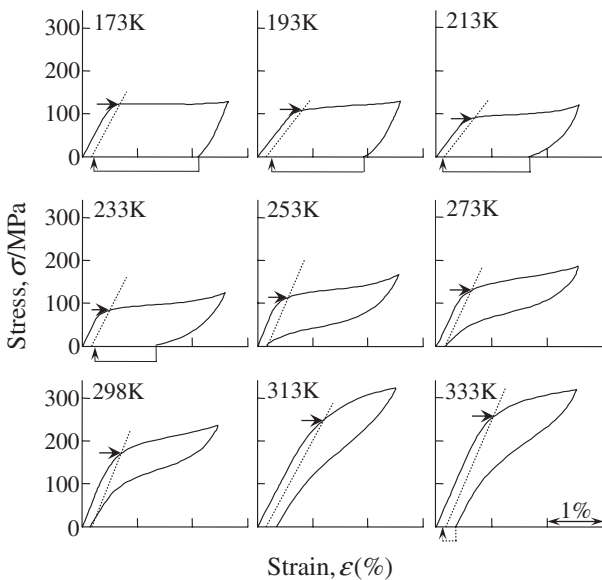


Fig. 9 Stress-strain curves obtained at various temperatures in the specimen annealed at 873 K.

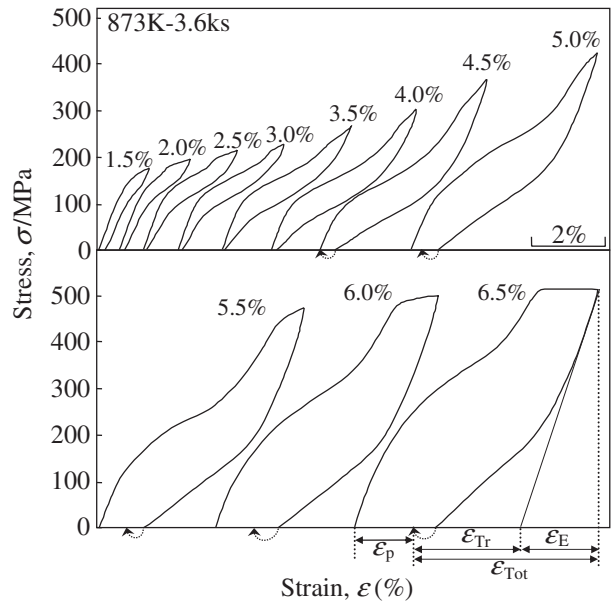


Fig. 11 Stress-strain curves obtained by cyclic loading-unloading tensile tests in the specimens annealed at 873 K.

be characterized by the critical stress ( $\sigma_s$ ) for slip, the maximum total recovery strain ( $\epsilon_{Tot}^{max}$ ) and the maximum recovery transformation strain ( $\epsilon_{Tr}^{max}$ ). The  $\sigma_s$  indicated by a white-headed arrow is defined in this study as the stress where 0.5% plastic strain is induced, while the  $\epsilon_{Tot}^{max}$  indicated by a dashed arrow is the maximum total recovery strain and the  $\epsilon_{Tr}^{max}$  indicated by a black-headed arrow is the maximum recovery transformation strain as shown in Fig. 12. The  $\sigma_s$  is estimated to be about 460 MPa, while the  $\epsilon_{Tot}^{max}$  and  $\epsilon_{Tr}^{max}$  to be 4.9 and 2.8%, respectively.

The  $\sigma_s$ ,  $\epsilon_{Tot}^{max}$  and  $\epsilon_{Tr}^{max}$  of the specimens are plotted against annealing temperature in Fig. 13. As shown in this figure, the  $\epsilon_{Tot}^{max}$  and  $\epsilon_{Tr}^{max}$  are almost constant irrespective of the annealing temperature. This indicates that the annealing temperature less affect the transformation strain. However,

the  $\sigma_s$  decreases with increasing annealing temperature from 560 MPa at 823 K to 315 MPa at 1173 K.

In order to apply Ti-based alloys to medical uses, the stability of superelasticity near body temperature is important. Cyclic tensile tests were carried out at room temperature. The specimens were elongated up to 2.5% strain followed by unloading at each cycle. The results for the specimens annealed at (a) 823 K, (b) 873 K and (c) 973 K are shown in Fig. 14. All the specimens show an excellent superelasticity. In particular the specimen annealed at 823 K exhibits superior superelastic behavior with a narrow stress hysteresis as shown in Fig. 14(a). Although the first curve exhibits incomplete superelastic recovery with a plastic strain

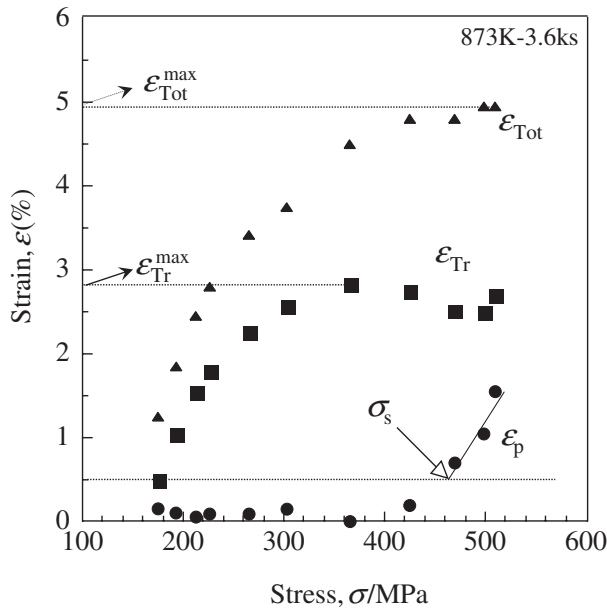


Fig. 12 Plastic strain ( $\epsilon_p$ ), total recovery strain ( $\epsilon_{Tot}$ ) and transformation recovery strain ( $\epsilon_{Tr}$ ) plotted against tensile stress in the specimen annealed at 873 K.

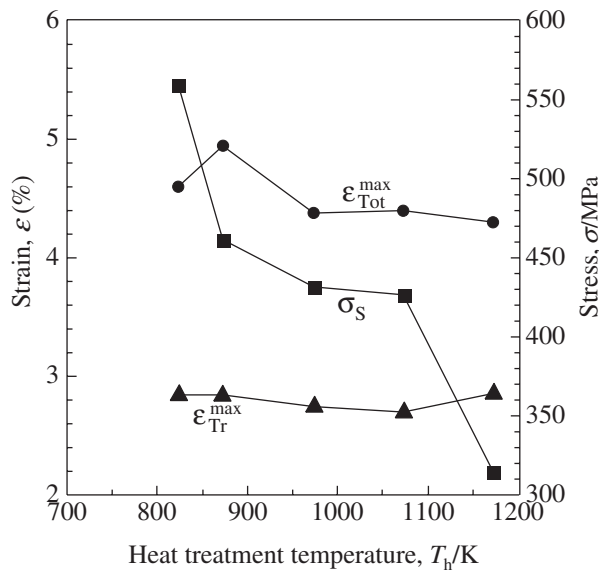


Fig. 13 Annealing temperature dependence of critical stress for slip ( $\sigma_s$ ), maximum total recovery strain ( $\epsilon_{Tot}^{max}$ ) and maximum recovery transformation strain ( $\epsilon_{Tr}^{max}$ ) in the specimens annealed at temperatures between 823 and 1173 K.

of 0.2%, the curves after the 2nd cycle exhibit almost complete superelastic recovery. The yield stress indicated by an arrow decreases from 295 MPa at the first cycle to 270 MPa at the third cycle, then it becomes almost constant irrespective of increasing cyclic number. It is clear that this yield stress is higher than those of the specimens annealed at 873 and 973 K. This is caused by the increase in the stress for inducing martensites due to the presence of  $\alpha$  phase and fine subgrain structure for the specimen annealed at 823 K as shown in Figs. 3 and 4.

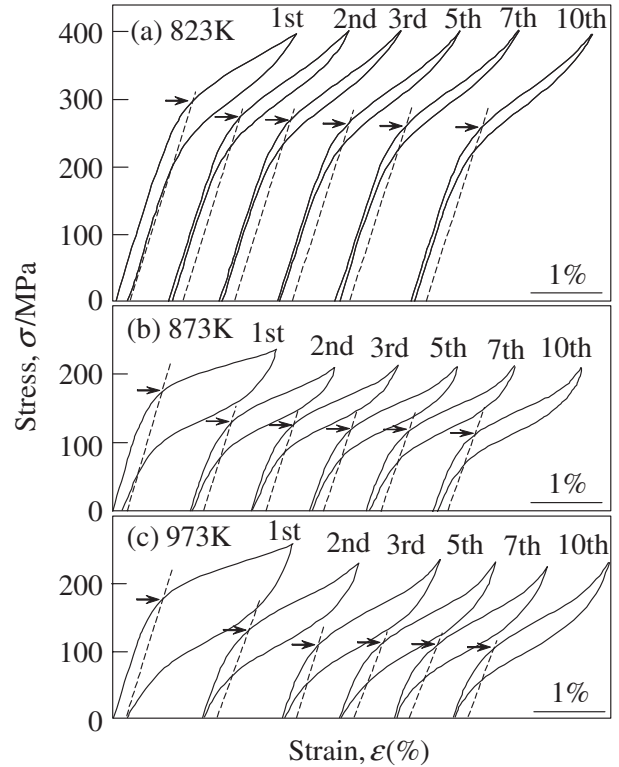


Fig. 14 Stress-strain curves obtained by repeated loading to the maximum strain of 2.5% followed by unloading at room temperature in the specimens annealed at (a) 823 K, (b) 873 K and (c) 973 K.

### 3.3 Relation between microstructure and shape memory properties

The change of microstructure with increasing annealing temperature for the Ti-22Nb-6Zr alloy is summarized as follows. (1) The specimens annealed above 873 K exhibited the fully recrystallized structure while the specimen annealed at 823 K exhibited the fine subgrain structure. The grain size increased with increasing annealing temperature. (2) The texture changed from the  $\{100\}\langle 110\rangle$  deformation texture to the  $\{112\}\langle 110\rangle$  recrystallization texture with increasing annealing temperature. It is noted that the rolling direction is parallel to  $\langle 110\rangle$  crystal directions in both textures. Thus, it is supposed that the effect of the texture change on mechanical properties is small in this study because the tensile direction is parallel to the rolling direction in all specimens. (3) The  $\alpha$  precipitates were observed in the specimens annealed at 773 and 823 K while they were dissolved in the specimens annealed above 823 K. As shown in Fig. 5, the fine athermal  $\omega$  phase formed by quenching was observed in all specimens, indicating that the athermal  $\omega$  phase is not related to the change of shape memory properties.

As mentioned above, the critical stress for slip ( $\sigma_s$ ) decreased with increasing annealing temperature. The specimen annealed at 823 K exhibited very high  $\sigma_s$  of 560 MPa, due to the  $\alpha$  precipitates and fine subgrain structure. The drastic decrease in  $\sigma_s$  with increasing annealing temperature from 823 to 873 K is due to the recrystallization and dissolution of  $\alpha$  precipitates. On the other hand, it is supposed that the decrease in  $\sigma_s$  between 873 K and 1173 K is

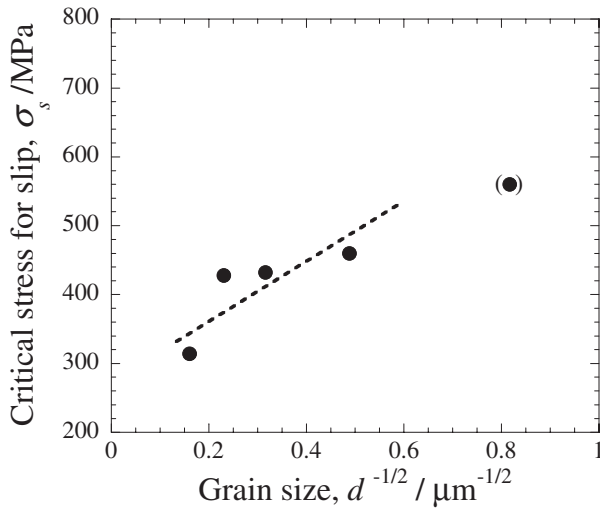


Fig. 15 Critical stress for slip ( $\sigma_s$ ) as a function of grain size ( $d^{-1/2}$ ) in the Ti-22Nb-6Zr(at%) alloy.

originated from the increase in grain size. Generally speaking, the Hall-Petch relationship,<sup>20,21)</sup> has been applied to polycrystalline aggregates to explain the relationship between yield stress  $\sigma_y$  and grain size  $d$ .

$$\sigma_y = \sigma_0 + k_y d^{-1/2} \quad (1)$$

where  $\sigma_0$  is a lattice friction stress and  $k_y$  is the slope of the Hall-Petch relationship. The Hall-Petch slope  $k_y$  depends on the resistance of grain boundaries to dislocation motion across the boundaries. It is expected that this relationship can be also applied to the relationship between the critical stress for slip and grain size in shape memory alloys. The critical stress for slip ( $\sigma_s$ ) is plotted against grain size ( $d^{-1/2}$ ) in Fig. 15. The grain size of the closed circle in parentheses is an average diameter of subgrains estimated in TEM micrographs. It is seen that the Hall-Petch relationship qualitatively holds between the critical stress for slip and grain size. The Hall-Petch slope in this study is estimated at about  $0.4 \text{ MN/m}^{3/2}$ . Further research is required to determine the  $\sigma_0$  and  $k_y$  precisely. It has been reported in literature that the value of  $k_y$  is  $0.25 \text{ MN/m}^{3/2}$  in a  $\alpha$ -Ti<sup>22)</sup> and  $0.37 \text{ MN/m}^{3/2}$  in a Ti-15.2 at%Mo alloy,<sup>23)</sup> respectively, suggesting that the value of  $0.4 \text{ MN/m}^{3/2}$  in the Ti-22Nb-Zr alloy is considerably reasonable. Up to date, the quantitative researches on the effect of grain size on shape memory properties have hardly been reported. This present study revealed that grain refinement is a very effective method in order to improve the shape memory and mechanical properties in  $\beta$ -type Ti-based alloys.

#### 4. Summary

The specimen annealed at 823 K for 3.6 ks exhibited a fine subgrain structure. A bimodal grain structure with a fine subgrain and recrystallized grain was observed in the specimen annealed at 873 K for 3.6 ks, while a fully

recrystallized structure was observed in the specimens annealed above 873 K. The grain size increased with increasing annealing temperature. The annealing temperature slightly affected the transformation temperature and recovery strain. However, the critical stress for slip decreased considerably with increasing annealing temperature, because the grain size increased with increasing annealing temperature. The specimen annealed at 823 K exhibited excellent superelasticity due to fine subgrains and  $\alpha$  precipitates. The Hall-Petch relationship holds between the critical stress for slip and grain size in the Ti-22Nb-6Zr(at%).

#### Acknowledgments

This work was partially supported by the ILC Project from University of Tsukuba the 21 Century Center of Excellence Program and the Grants-in-Aid for Fundamental Scientific Research Kiban A (1999–2001), Kiban A (2002–2004) from the Ministry of Education, Culture, Sports, Science and Technology, Japan.

#### REFERENCES

- 1) S. Shabalovskaya: Proc. First Inter. Conf. Shape Memory and Superelastic Technologies, 1994, 209.
- 2) T. W. Duerig, J. Albrecht, D. Richter and P. Fischer: Acta Metall. **30** (1982) 2161–2172.
- 3) W. F. Ho, C. P. Ju and J. H. Chern Lin: Biomaterials **20** (1999) 2115–2122.
- 4) T. Grosdidier and M. J. Philippe: Mater. Sci. Eng. A **291** (2000) 218–223.
- 5) H. Hosoda, N. Hosoda and S. Miyazaki: Trans. MRS-J **26** (2001) 243–246.
- 6) H. Y. Kim, Y. Ohmatsu, J. I. Kim, H. Hosoda and S. Miyazaki: Mater. Trans. **45** (2004) 1090–1095.
- 7) T. Maeshima and M. Nishida: Mater. Trans. **45** (2004) 1096–1100.
- 8) T. Maeshima and M. Nishida: Mater. Trans. **45** (2004) 1101–1105.
- 9) C. Baker: Mater. Sci. J. **5** (1971) 92–100.
- 10) H. Y. Kim, S. Hashimoto, J. I. Kim, H. Hosoda and S. Miyazaki: Mater. Trans. **45** (2004) 2443–2448.
- 11) K. Nitta, S. Watanabe, N. Masahashi, H. Hosoda and S. Hanada: Structural Biomaterials for the 21st Century, (TMS, 2001) 25–34.
- 12) H. Hosoda, Y. Fukui, T. Inamura, K. Wakashima, S. Miyazaki and K. Inoue: Mater. Sci. Forum **425–432** (2003) 3121–3124.
- 13) T. Inamura, Y. Fukui, H. Hosoda, K. Wakashima and S. Miyazaki: Mater. Sci. Eng. C **25** (2005) 426–432.
- 14) J. I. Kim, H. Y. Kim, H. Hosoda and S. Miyazaki: Mater. Trans. **46** (2005) 852–857.
- 15) J. I. Kim, H. Y. Kim, T. Inamura, H. Hosoda and S. Miyazaki: Mater. Sci. Eng. A. **403** (2005) 334–339.
- 16) S. G. Steinemann: Evaluation of Biomaterials, Ed. By G. D. Winter, J. L. Leray and K. de Goot, (John Wiley & Sons, Ltd., 1980) 1–34.
- 17) H. Y. Kim, T. Sasaki, K. Okutsu, J. I. Kim, T. Inamura, H. Hosoda and S. Miyazaki: Acta Mater. **54** (2006) 423–433.
- 18) T. Inamura, Y. Fukui, H. Hosoda, K. Wakashima and S. Miyazaki: Mater. Trans. **45** (2004) 1083–1089.
- 19) D. L. Moffat and D. C. Larbalestier: Metall. Trans. A **19A** (1988) 1687–1694.
- 20) E. O. Hall: Proc. Phys. Soc. Lond. **B64** (1951) 747–753.
- 21) N. J. Petch: J. Iron Steel Inst. **174** (1953) 25.
- 22) H. Conrad: Prog. Mater. Sci. **26** (1981) 123–403.
- 23) K. H. Chia, K. Jung and H. Conrad: Mater. Sci. Eng. **409** (2005) 32–38.